Journal of Physics D:
Applied Physics

PAPER • **OPEN ACCESS**

Ultralow-threshold single-mode quantum-dot laser operating at O-band based on bound-states in the continuum

To cite this article: Danqi Lei *et al* 2025 *J. Phys. D: Appl. Phys.* **58** 415105

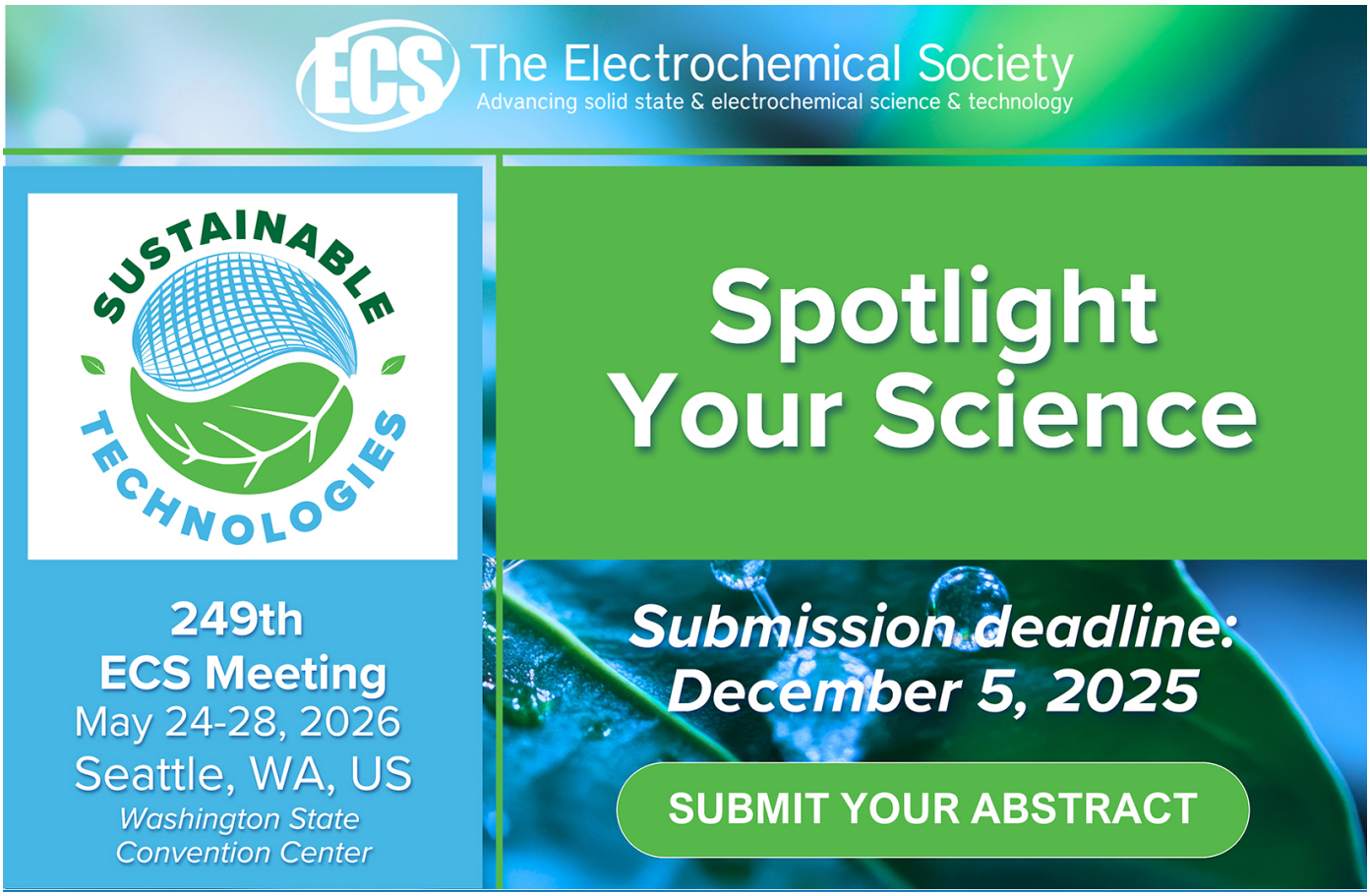

OPEN ACCESS
IOP Publishing
Journal of Physics D: Applied Physics
J. Phys. D: Appl. Phys. **58** (2025) 415105 (12pp)
https://doi.org/10.1088/1361-6463/ae0b80

Ultralow-threshold single-mode quantum-dot laser operating at O-band based on bound-states in the continuum

Danqi Lei[1,7], Ji Tong Wang[1,2,7], Bogdan-Petrin Ratiu[3], Huiwen Deng[1], Xuanchang Zhang[1], Zhao Yan[3], Suguo Huo[4], Liwei Cao[5], Wei Li[5], Siming Chen[6], Qiang Li[3], Huiyun Liu[1], Nicolae C Panoiu[1] and Mingchu Tang[1,*]

[1] Department of Electronic and Electrical Engineering, University College London, Torrington Place, London WC1E 7JE, United Kingdom
[2] Wuzhen Laboratory, EGO Wuzhen Digital, Economy Industrial Park, No. 925 Daole Road, Tongxiang City, People's Republic of China
[3] School of Physics and Astronomy, Cardiff University, Cardiff CF24 3AA, United Kingdom
[4] London Centre for Nanotechnology, 17-19 Gordon Street, London WC1H 0AH, United Kingdom
[5] Institute of the Microstructure and Properties of Advanced Materials, Beijing University of Technology, Beijing 100124, People's Republic of China
[6] Laboratory of Solid State Optoelectronics Information Technology, Institute of Semiconductors, Chinese Academy of Sciences, Beijing 100083, People's Republic of China

E-mail: mingchu.tang@ucl.ac.uk, smchen@semi.ac.cn and n.panoiu@ucl.ac.uk

Received 24 July 2025, revised 19 September 2025
Accepted for publication 25 September 2025
Published 8 October 2025

Abstract

Light sources for generation of optical angular momentum (OAM) are popular on telecommunication systems and in demand for key telecommunications platforms, including on-chip ultra-compact integrated communication systems, free-space optical communication and optical fiber networks. Here, we demonstrate an ultralow-threshold laser based on optical bound states in the continuum (BIC), which serves as an ideal light source for generation of beams with OAM. In this context, given semiconductor material stability and robustness, the proposed BIC laser, comprising an InAs/GaAs quantum-dot (QD) active region and lasing at a wave-length of $\sim$1.3 μm, is characterized by a power threshold of 7.5 μW (0.038 kW cm^{-2}) at room temperature. Moreover, our experimental measurements and computational analysis of the generated optical field reveal the vortex nature of the optical beam, as well as its non-trivial topological properties. This work demonstrates an energy-efficient, stable, and versatile single-mode QD BIC laser, which, as a source of optical vortex beams with large light extraction efficiency, offers great potential to facilitate high-capacity data transmission in future optical communication systems.

[7] These authors contributed equally to this work.
[*] Author to whom any correspondence should be addressed.

Supplementary material for this article is available online

Keywords: bound states in the continuum, orbital angular momentum, quantum dots, laser, vortex beam

1. Introduction

Optical beams carrying optical angular momentum (OAM) have attracted significant attention due to their use in many applications, including optical tweezers [1], quantum entanglement [2], nonlinear optics [3], high-resolution imaging [4], and optical communications [5–9]. The phase wavefront of OAM beams is helical, which leads to a phase singularity at the center of OAM beams [7, 10]. The azimuthal variation of the electric field profiles of an OAM mode can be represented by its topological charge. OAM beams with different topological charge are orthogonal to each other [5, 11, 12]. This orthogonality is particularly advantageous in optical communication systems, where OAM modes can serve as independent carrier channels to enhance transmission capacity of wavelength division multiplexing systems. Specifically, OAM provides an additional degree of freedom, namely the angular momentum quantum number, which can be used in communication systems to efficiently multiplex/demultiplex optical transmission channels [6–9]. Such optical communication systems possess high data capacity and significantly reduced unwanted crosstalk effects among transmission channels [10, 13]. OAM light sources can play an important role in different types of communication systems, including optical fiber networks [7], free space optical communication [14], and compact integrated communication systems [15, 16].

On the downside, conventional OAM beams are generated through complex set-ups, including spiral waveguides [17] or intricate computer generated holograms [13, 18], which can degrade the system efficiency and reliability. As an alternative, semiconductor-based vortex beam lasers that generate light beams carrying OAM directly provide on-chip light sources with engineered topological charge. Therefore, an on-chip bound state in the continuum (BIC) laser that naturally emits a vortex beam with OAM can provide key advantages if used in next-generation data communication systems [8, 19]. Currently, miniaturized on-chip lasers based on III–V semiconductors materials, including defect cavity lasers [20], nanoscale coaxial lasers [21], micro-disk lasers [22, 23], attract enormous interest, owing to their compactness, low-power consumption, and wide emission range [24]. Among these, BIC lasers deliver vortex beams [25–30] due to their intrinsic physical properties.

On-chip BIC lasers have developed from the concept of BIC modes with OAM and none-zero topological charge [31–33]. These are localized optical modes located in the continuum but completely decoupled from the radiative modes, leading to an infinity quality factor, Q. In addition, these symmetry-protected BIC modes located at the Γ-point are particularly stable against perturbations upon free-space propagation as they are characterized by integer topological invariants, i.e. the topological charge quantifying the OAM of the beam [34]. Equally important, BIC lasers implemented in a photonic crystal (PhC) configuration can have ultra-small footprint and low-power consumption, and therefore play an important role in photonic integrated circuits [25–30].

For such miniaturized device, the selection of active region material is critical in the design of the emission frequency and lasing characteristics. To this end, InAs/GaAs quantum-dot (QD) material is an ideal candidate, owing to its wide gain spectrum covering telecommunication wavelengths (O-band) and its delta-function like density of state that contributes to large frequency separation [35]. Moreover, because of its temperature stability property [36]. InAs QD material greatly alleviates the issue of large heat dissipation rate in a small-volume cavity. Furthermore, due to their unique property of being unaffected by crystal defects generated during the III–V/Si heteroepitaxial growth [20, 37], self-assembled InAs QD materials provided an effective approach towards the development of Si-based, on-chip light sources [38].

Here, we developed a QD BIC laser on III–V material platform, which exhibits a single mode at $\sim$1.3 μm and generates optical vortex beams. An optical system design has been demonstrated, whereby a set of optical modes at the pump frequency ensures highly effective optical pumping via enhanced in-coupling of light, whereas the single-mode feature across the gain spectral range leads to particularly efficient light extraction. This innovative laser design allowed us to observe an ultralow threshold power of 7.5 μW (0.038 kW cm^{-2}) at room temperature and lasing wavelength of $\sim$1.3 μm (precisely at 1254 nm) within *O*-band, which to the best of our knowledge represents the lowest threshold of a BIC laser based on GaAs platform reported to date in the literature [26, 29, 39]. This ultralow threshold is comparable with that of BIC devices implemented on other platforms, including perovskite films [27, 40, 41], InP substrate [25, 42], colloidal nanoplatelets [28, 43], and GaN substrate [30]. The experimentally measured characteristics of this nano-laser agree very well with our simulated results and theoretical modeling. As designed, a vortex beam with a doughnut shape intensity is generated by our five-layer QDs BIC laser. This vortex beam has been characterized by comparing the measured and simulated far-field profiles observed under different polarization conditions. This dual-frequency cavity design delivers excellent confinement of light at the pump and lasing frequencies, thus resulting in a BIC laser that generates vortex beams with ultralow optical power.

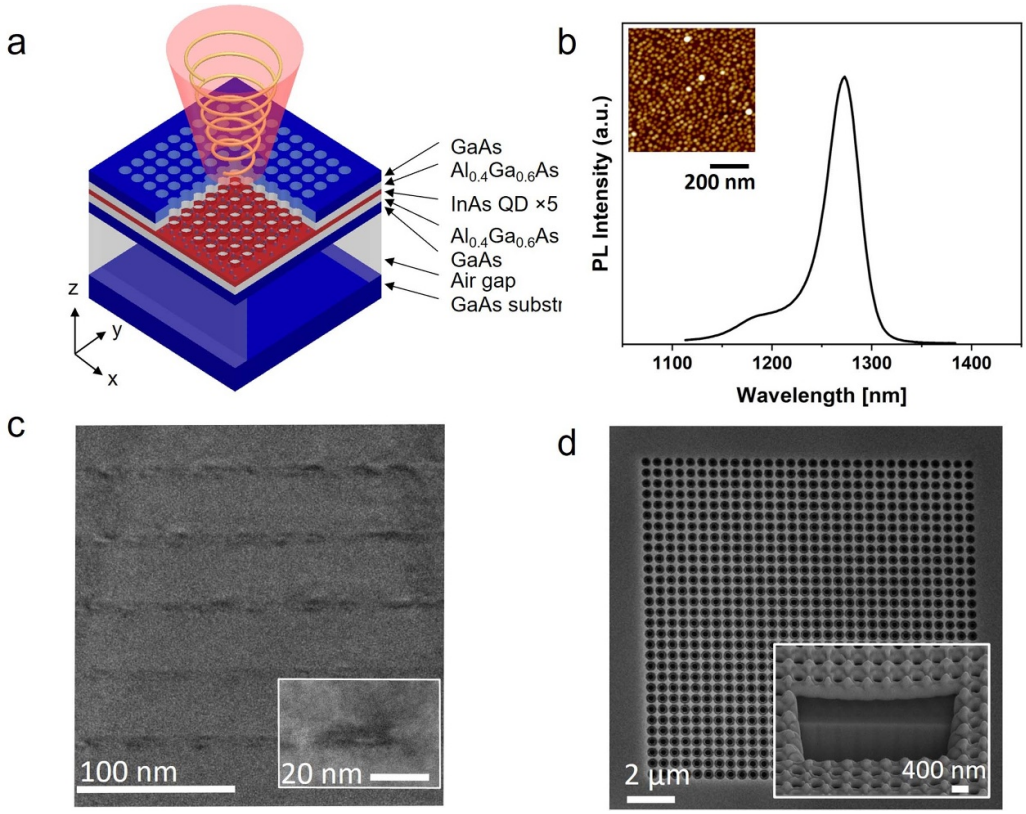

Figure 1. QD BIC laser structure. (a) Schematic of the fabricated BIC laser showing a vortex beam (red) generated vertically through the BIC cavity that is suspended on the GaAs substrate. (b) A PL spectrum of five layers of DWELL structure illustrates a FWHM of 30.11 meV. Inset: an image showing the QD distribution, measured to have a density of 5 $\times$1010 cm^{-2}. (c) A cross-section TEM image of the 5 layers DWELL structure without visible defect. Inset: image of a single QD with a height of $\sim$ 5 nm and a diameter of $\sim$20 nm. (d) A SEM image of the fabricated BIC laser. It consists of 30 by 30 square lattice units with a lattice constant of 500 nm, a hole radius of $\sim$238 nm and a sidewall slope of 17.5°. Inset: a SEM cross-section image taken at the device center, showing the 616 nm air gap formed underneath the PhC membrane.

2. Methods

2.1. Material epitaxy and device fabrication

The InAs/GaAs QD BIC laser wafer was grown on an n-type doped GaAs substrate using solid-source Veeco GEN930 molecular beam epitaxy system, as shown in figure 1(a). After a 200 nm GaAs buffer layer growth, the laser structure begins with a layer of 1000 nm $Al_{0.8}$ $Ga_{0.2}As$ as the sacrificial layer, followed by a 30 nm $Al_{0.4}Ga_{0.6}As$ layer serving as the waveguiding. The active region is sandwiched by two layers of GaAs with thickness of 38.5 nm. Within the active region lies a conventional five layers of dot-in-well (DWELL) structure [44], which includes a layer of 2 nm of $In_{0.16}Ga_{0.84}As$ underneath the QD and a layer of 4 nm $In_{0.16}Ga_{0.84}As$ on top of the QD. Each adjacent DWELL structure is separated by a 38.5 nm GaAs spacer layer grown at high temperature. The laser structure is completed by an additional layer of 60 nm $Al_{0.4}Ga_{0.6}As$ forms the upper waveguiding layer above the GaAs and followed by a layer of 10 nm GaAs.

A photoluminescence (PL) spectrum of the QD material is used to examine the quality of QD, which is shown in figure 1(b). It possesses a full width at half maximum (FWHM) of 30.11 meV (46 nm) and a gain peak at $\sim$1.3 μm. The QD surface morphology has been characterized by atomic force microscopy. As shown in the inset of figure 1(b), the QD density is $\sim$5 $\times 10^{10}$/cm^2 per layer, namely, it is comparable with the value reported in the literature for other InAs/GaAs QD materials. To further describe the QD material morphology, we analyzed the sample using transmission electron microscopy (TEM), as per figure 1(c). The inset of figure 1(c) shows one of the InAs QDs; it is a flat disk with diameter of $\sim$ 20 nm and height of $\sim$5 nm. Such dot shape favors optical coupling with a TE-polarized near-fields [35].

The BIC PhC structure is fabricated by utilizing Elionixe G100 electron-beam lithography to write the desired pattern on a layer of 120-nm thick e-beam negative resist, HSQ, coated on the wafer, which turns to SiO_2 after exposure and serves as a hard mask. A dry etching step is performed by an inductively coupled plasma reactive ion etching (ICP) facility to transfer the pattern onto the QD material. The suspended membrane configuration is achieved through wet etching, which removes the sacrificial layer underneath the QD active region by using a 48% hydrofluoric acid solution for 10 s (see figure S5 in supplementary information (SI) for fabrication details). Zeiss XB1540 scanning electron microscopy (SEM) image of the fabricated BIC laser is presented in figure 1(d), which shows the fabricated PhC structure with a 30 by 30 periods. This PhC

structure contains a lattice constant of 500 nm, a hole radius of 238 nm and a sidewall slope of 17.5°. Therefore, simulation work has been carried out to study the Q-factor and wavelength of the BIC mode on θ, as per figure S6 of the supplementary information (SI). It has been found that, as expected, the BIC nature is not affected by the change of θ, whereas the resonance wavelength remains roughly within the gain spectrum when θ varies from 0° to 25°. A focus ion beam is used to cut a 4.5 μm × 2.5 μm window with about 2 μm depth and its corresponding SEM cross-section image included in figure 1(d) as inset illustrates an air gap with a thickness of 616 nm. In addition, a slight surface bending is observed in this SEM cross-section image. It is caused by an undesired expansion in the sacrificial layer that contains a large Al composition. However, such surface bending issues can be mitigated by reducing the Al composition in the sacrificial layer so as to slow the etching rate. Finally, the device is completed after rinsing off the photoresist with Acetone followed by an O_2 hazing for 5 min.

2.2. Laser structure simulation

The laser configuration presented in this work was developed by properly designing the optical mode properties of a free-standing PhC structure. Specifically, we were guided by the following three design principles: i) a single-lasing mode exists within the gain spectrum of InAs/GaAs QD material; ii) there is a large spectral/spatial overlap between the lasing mode and QD material; and iii) in all simulations we considered the values of the device parameters to be those of the actual fabricated devices. In this design process, we considered both an infinite PhC structure as well as a finite one. The design process commenced with the investigation of the optical response of the device, by computing the band structure of an infinite-size PhC slab. In these computations, the finite-element method implemented in COMSOL Multiphysics was employed [45]. To simplify the numerical calculations, the refractive index of the materials in the layered photonic structure was set to be the same for all layers in the slab ($n = 3.4$). This is a valid approximation given that the index of refraction varies across the layers by less than 5%. In addition, despite the broken up-down mirror symmetry introduced during fabrication by the etching process, the modes of the PhC slab can still be classified into TE-like (TM-like) when the electric (magnetic) field lies predominantly in the plane of the slab. Moreover, the in-plane inversion symmetry of the PhC slab allows one to separate the optical resonances of the slab located at the Γ-point into symmetry-protected BICs with infinite Q-factor and guided lattice resonances with finite Q-factor.

Based on these considerations, figure 2(a) presents the calculated band structure of the PhC slab, within the spectral range of interest. This figure shows that within the spectral range of the optical gain of the QD material (mauve region), there exists one TE-like mode and two TM-like modes. Since the QDs in the gain layers couple more effectively with the TE-like modes [46], here we primarily focus on the TE-like mode with wavelength of 1270 nm at the Γ-point. The near-field profile of this mode is given in the inset of figure 2(a) and it clearly shows a strong overlap between electric field and active material. Next, to demonstrate the topologically nontrivial nature of this TE-like mode, its Q-factor map was determined in the momentum space and the corresponding far-field polarization at a set of k-points, as presented in figure 2(b). It can be clearly seen that the Q-factor diverges at the Γ-point, whereas the far-field polarization (green short lines) winds around the Γ-point along a closed k-path and produces a 2π phase accumulation. This indicates the existence of a BIC with topological charge of $+1$. Note that, as expected, the far-field polarization becomes ill-defined at the Γ-point.

The fabricated structure had a finite size, so that one expects that finite size effects would influence the optical properties of the generated optical beam. To understand this interplay between the device size and the nature of the lasing optical mode, the eigenmodes of a 15 ×15 unit cell PhC slab were numerically investigated. In choosing this number of unit cells we have been guided by the size of the pump beam used in the experiment, that is, an optical beam with diameter of about 5 μm. The results of this analysis are summarized in figure 2(c), where we present the spatial distribution of the electric field amplitude of the BIC lasing mode, determined in the (x,y)-plane passing through the middle of the finite-size PhC slab. Note that the field profile inside a unit cell of the finite-size PhC slab is similar to that corresponding to a unit cell of an infinite PhC slab shown in figure 2(a). Moreover, due to the inherent radiative losses associated with a finite-size PhC structure, the Q-factor of the BIC of the finite-size PhC slab is reduced to 707.

A deeper understanding of the nature of the lasing optical mode of the finite-size PhC slab can be gained from the Fourier analysis of the optical near-field determined in an (x,y) -plane located just above the PhC slab. The main conclusions of this analysis are collated in figure 2(d). In particular, the Fourier transform of the optical near-field is plotted in the (k_x,k_y) -plane in this figure. This plot reveals several important ideas. Firstly, the optical field comprises two parts, namely propagating plane waves that correspond to the interior of the circle defined by the equation ${k_x}^2 + {k_y}^2 = {\omega_0}^2/c^2$ (green circle), and evanescent (decaying) plane waves that correspond to the region outside this circle, where, ω_0 is the frequency of the BIC mode at the Γ-point. As only the propagating plane waves carry energy into the far-field region, one can readily determine the spatial distribution of the far-field lasing mode. Secondly, the small dark region centered at the Γ-point indicates vanishing far-field emission along the out-of-plane direction ($+z$ -axis), a fact that confirms the existence of a BIC. Due to the finite-size effects, one can also observe a series of side lobes along k_x - and k_y -axis. Finally, the bright spots located outside the green circle and forming a square lattice correspond to the evanescent optical nearfield.

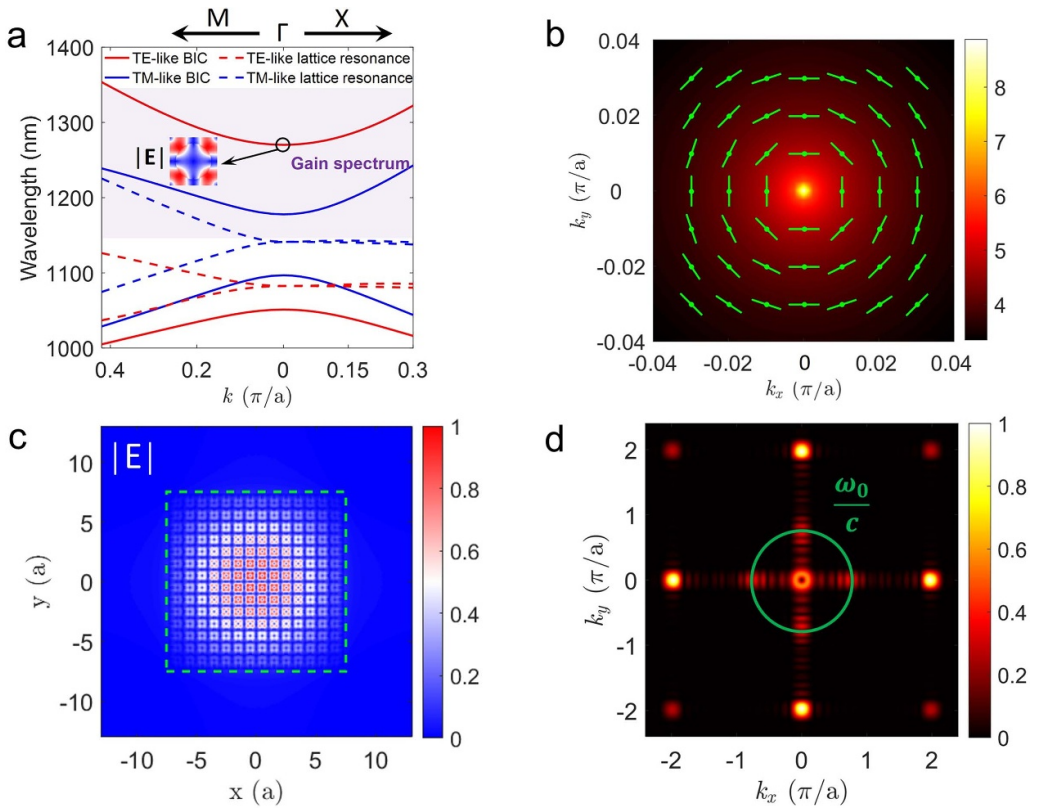

Figure 2. Characteristics of the BIC in the periodic and finite-size structures. (a) Calculated photonic band structure of a periodic square-lattice PhC slab. The mauve-shaded region indicates the spectral range of the gain of the QD material. Inset: The distribution of the electric field amplitude of the TE-like BIC with wavelength of 1270 nm at the Γ-point. (b) Calculated Q-factor ($\log Q$) map. The green short dashes indicate the direction of the electric field polarization at the k-points marked by dots. (c) Distribution of the electric field amplitude calculated in the cross-section corresponding to the middle of a slab consisting of 15 ×15 unit cells. The green dashed line denotes the boundary of the PhC region. (d) The Fourier transform of the optical near-field computed just above the finite-size PhC slab. The green circle is defined by ${k_x}^2 + {k_y}^2 = {\omega_0}^2/c^2$, where ω_0 is the angular frequency of the BIC supported by the finite-size slab and c is the speed of light in vacuum. The points inside (outside) this circle correspond to propagating (evanescent) plane waves.

3. Results

To assess the characteristics of the fabricated device, this QD BIC laser is characterized by a micro photoluminescent (μ-PL) measurement set-up (diagram of the μ-PL set-up is shown in figure S7). A continuous wave (CW) HeNe laser emitting at 633 nm (Thorlabs HNLS008R-EC) is directed towards an infinity corrected objective lens which focuses the light onto the sample in a circular beam spot with a diameter of 5 μm. Details of this measurement set-up can be seen in supplementary materials. Figure 3 presents the measurement results, demonstrating device emission wavelength and lasing properties. A series of normalized spectra corresponding to increasing values of the pump power are presented in figure 3(a). As it shows, a peak emerges at 1254 nm when the pump power is ∼7 μW then sharply rises as the pump power is further increased. The single-mode property is preserved during the entire operation range, up to seven times of the threshold power. No other peaks have been observed; however, the broad baseline grows slightly, owing to the enhanced spontaneous emission. The background spontaneous emission noise corresponds to the spontaneous emission component that did not couple into the lasing mode. A higher β-factor generally leads to a lower spontaneous noise in the background. It can be achieved by reducing the mode volume through optimized cavity design or size reduction, and by increasing the optical gain of the active region. In our case, incorporating more than five QD layers is a promising strategy to boost gain and further improve the β-factor in future devices.

A light–light (L–L) curve of this laser is illustrated in figure 3(b). A threshold of 7.5 μW (0.038 kW cm^{-2}) is determined by a linear fitting to the measurement data, which is the lowest threshold power (Shown in table 1) reported in the literature to date [25–30, 39–43, 47, 48]. This can be attributable to the spectral properties of the laser nearby the pump frequency and the QD materials gain characteristics. Thus, the cavity of the BIC laser was engineered not only for efficient emission, but also for enhanced in-coupling of the pump power by ensuring that there are multiple bands in the spectral range of the pump. More specifically, our device possesses in the proximity of the frequency of the pump a series of optical resonances (both BICs and waveguide leaky modes), which significantly increases the amount of power that is transferred from the pump to the active QD region (see figure S4 in SI). Moreover, by carefully aligning the electrical field, we were able to achieve lasing even for a relatively low value of the

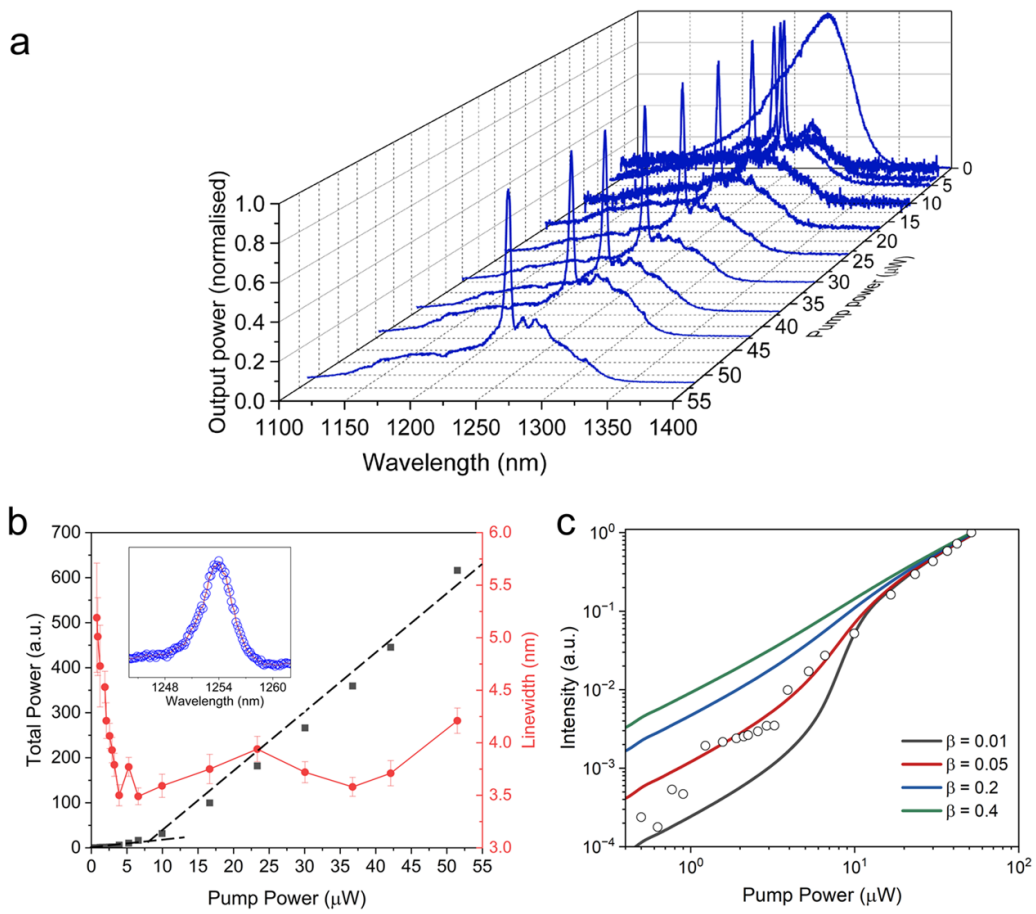

Figure 3. Characteristics of the QD BIC laser. (a) Normalized spectra as a function of pump power and wavelength for a 30-by-30 array BIC laser, which shows a single lasing peak at 1253.76 nm at a pump power of ∼7.5 μW at room temperature. (b) Integrated light intensity for the entire spectrum from 1100 nm to 1400 nm, and lasing linewidth fitted by Lorentzian model against pump power ranging from 0 to 55 μW. A lasing threshold of 7.5 μW is identified from the linear fitting dash lines (black), while the black square dots corresponding to y-axis at left are the measurement data. A red line represents the linewidth of the Lorentzian fitted spectrum associated with different pumping power. Inset: lasing spectrum measured at a pump power of 9.9 μW with a measured linewidth of 3.5 nm. (c) Logarithmic L–L curve of the BIC laser with measured data and simulated β value of 0.01, 0.05, 0.2, 0.4, which shows the β of 0.05 is the best fitted value.

threshold of 7.5 μW. The previous work [29] utilizes a QD material with 3 layers of QDs that is two layers less than the material we applied in this work. Therefore, by carefully aligning the electrical field profile with the gain material, a maximum overlap with the gain material and electrical field facilities lasing with a low Q factor. Figure 3(b) also presents the dependence of the linewidth of emission spectra on the pump power, obtained by fitting the emission spectra with a Lorentzian, which illustrates that the linewidth of the lasing mode decreases from 5.4 nm to 3.49 nm after lasing occurs. These linewidth measurements indicate a Q factor of 359. The inset in figure 3(b) depicts the spectrum measured at a pump power of 9.9 μW. It is noted that the Q-factor in this work is slightly lower than but comparable to that of most state-of-the-art BIC lasers [49–51]. To understand this, we investigate the dependence of Q-factor on the air gap thickness, and the results show that in the case of our device there exists significant energy leakage into the substrate when the air gap is equal to 616 nm (see figure S3 of the SI). Recently, it has been demonstrated that the Q-factor of BIC lasers can be enhanced by merging an accidental BIC mode with a symmetry-protected BIC mode [26] or by adding an optical medium around the laser cavity [29, 41] so as to enhance the lateral confinement. So far, the record-high Q-factor of BIC lasers [30] using QDs is ∼32 500. Regarding our work, there are several strategies that can further improve the Q-factor: (i) improve etching techniques to reduce surface roughness and structural disorder, thus lowering scattering loss; (ii) optimize air gap thickness to minimize the energy leakage into the substrate; and (iii) reduce side leakage by using photonic heterostructures with topological band inversion or using photonic bandgap boundaries.

Effective lasing requires strong confinement of the lasing optical mode inside the cavity and efficient stimulated emission within the active region. The β-factor, which quantifies the fraction of spontaneous emission coupled into the lasing mode, serves as a key indicator of laser efficiency [52]. To determine the parameter β of the fabricated BIC laser, we employed a commonly used model based on coupled rate equations [53]. According to this model, the dynamics of carrier density N and photon density P in the fabricated QD region

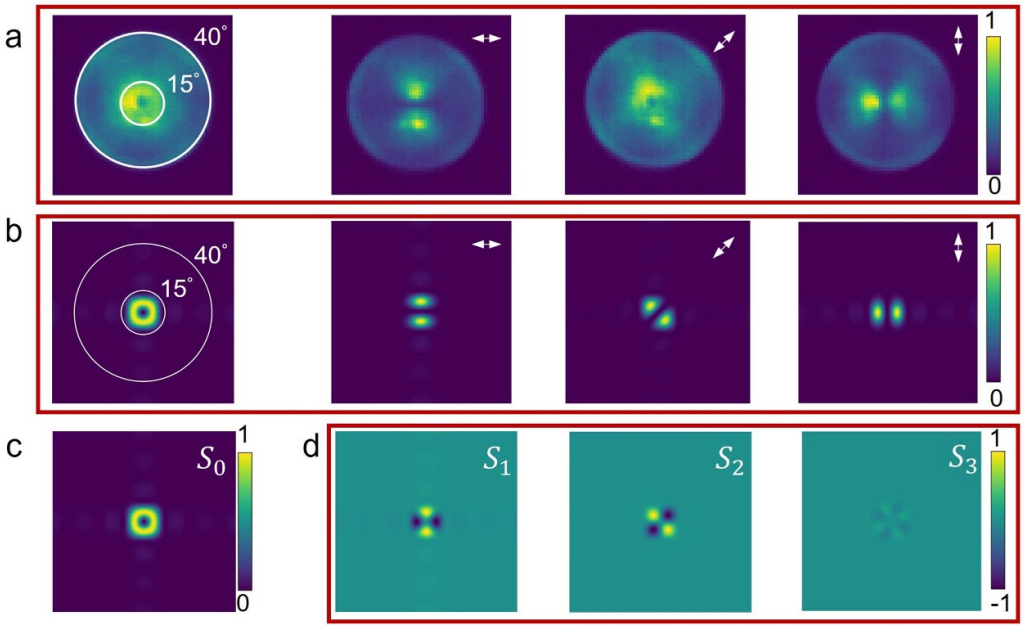

Figure 4. Measured (a) and simulated (b) far-field beam profiles of the QD BIC laser. The first panel of (a) shows the measured beam intensity, whereas the following panels show the polarization-resolved far-field beam profiles when the field polarization angle is selected to be 0°, 45°, and 90°, respectively. The simulated far-field patterns shown in, (b), illustrate the agreement with the measurement results. Stokes parameters determined from the simulated far-field of the finite-size PhC slab are presented in (c).

can be described by the following equations:

$$\frac{\mathrm{d}N}{\mathrm{d}t} = \frac{\eta P_\mathrm{p}}{\hbar\omega_\mathrm{p} V_\mathrm{a}} - \frac{N}{\tau_\mathrm{r}} - \frac{N}{\tau_\mathrm{nr}} - g\left(N\right)P \tag{1}$$

$$\frac{\mathrm{d}P}{\mathrm{d}t} = \Gamma g\left(N\right)P + \Gamma\beta\frac{N}{\tau_\mathrm{r}} - \frac{P}{\tau_\mathrm{p}} \tag{2}$$

where η is the absorption ratio of pumping power in the QD active region, P_p and ω_p are the power and frequency of the pump laser, respectively, $\hbar$ is the reduced Planck constant, V_a is the volume of the pumped active region, τ_r and τ_nr are the radiative and non-radiative recombination lifetime, respectively, $g(N)$ is the gain function, Γ is the confinement factor, and τ_p is the lifetime of the photons in the BIC. The non-radiative recombination processes, including the surface and Auger recombination processes, are much weaker than the radiative recombination process [53] and consequently the N/τ_nr term in equation (1) can be ignored. A linear gain function $g\left(N\right) = g_0\left(c/n_\mathrm{eff}\right)\left(N/N_\mathrm{tr} - 1\right)$ is assumed, where g_0 is the gain coefficient of the QD active medium, c is the speed of light in vacuum, n_eff is the effective refractive index of the PhC structure, and N_tr is the transparency carrier density.

Our calculations show that $\eta = 0.115$, $V_\mathrm{a} = 1.68 \times 10^{-19}$ m^3, $n_\mathrm{eff} = 2.32$, and $\Gamma = 0.062$. Moreover, $\tau_r = 1.58 \times 10^{-9}$ s [20], $\tau_\mathrm{p} = Q/\omega_0 = 2.42 \times 10^{-13}$ s, where Q is a measured Q -factor of the lasing mode and ω_0 is the peak lasing frequency, and the measured gain coefficient is $g_0 = 2100$ m^{-1} [35]. The steady-state solution of the rate equations can be found for a given value of β by setting the l.h.s. of equations (1) and (2) to zero and solving the resulting system of equations for N and P. Then, the output power is calculated as $P_\mathrm{out} = \hbar\omega_0 P V_\mathrm{mode}/\tau_\mathrm{p}$, where $V_\mathrm{mode} = V_\mathrm{a}/\Gamma$ is the optical mode volume. The results of this simple analysis are shown in figure 3(c), where we present the $P_\mathrm{out}\left(P_\mathrm{p}\right)$ curves corresponding to $\beta = 0.01, 0.05, 0.2, 0.4$, as well as the measured data. It can be seen in this figure that the best fit of the experimental data is achieved for $\beta = 0.05$ and $N_\mathrm{tr} = 1.12 \times 10^{20}$ m^{-3} for this QDs BIC laser. The estimated β of the laser is comparable to the state-of-the-art BIC-based lasers reported to date [26, 29, 41, 54].

The phase of optical vortices with topological charge $+1$ undergoes a variation of 2π upon circling once the center of the vortex, which translates to a doughnut shape of the intensity of the optical far-field profile [55]. To explore the properties of the optical beam generated by our QD BIC laser, a set of far-field measurements have been carried out with a spectrometer (Acton SpectraPro SP-2750) set at zeroth order diffraction, serving as a CCD camera. The far-field patterns of our QD BIC laser at a pump power of 51 μW (above lasing) are examined. As shown in the first panel of figure 4(a), a doughnut shaped far-field is observed with a divergence angle of $\sim$15°. It reveals that a vortex beam is generated from the QD BIC laser. Here, 40° is the maximum divergence angle that could be detected with our set-up. To examine the polarization property of the lasing beam, the far-field profile is measured after it passed through a polarizer. As shown in the following three panels in figure 4(a), the far-field now consists of two rotating lobes

when the polarizer is along horizontal (0°), diagonal (45°) and vertical (90°) directions.

Comparing the measured and simulated polarization-resolved far-field beam profiles presented in the panels of figures 4(a) and (b), respectively, a good agreement between the experimental and theoretical predictions is observed. It confirms that a vortex beam is generated by our QD BIC laser.

4. Conclusion

In summary, we have observed a $\sim$1.3 μm vortex beam with topological charge of $+1$ generated by a QD BIC laser consisting of square lattice PhC slab with 30 $\times$30 units. The performance characteristics of our fabricated QD BIC laser including single mode emission, doughnut shape of the optical far-field profile, and high spontaneous coupling efficiency, have been determined experimentally and validated by numerical simulations. In our design, a TE polarized symmetry-protected BIC mode at Γ-point of the PhC has been used as a lasing mode. Importantly, our CW pumped QD BIC laser obtains an ultra-low threshold of 7.5 μW (0.038 kW cm^{-2}) at room temperature without a lateral confinement structure. To best of our knowledge, to date this represents the lowest threshold (shown in table 1) of BIC lasers reported in the literature [25–30, 39–43, 47, 48].

Table 1 summarizes the characteristics of BIC lasers reported in literature, namely their pumping condition, gain material, threshold power density, device size and lasing wavelength. BIC lasers have been demonstrated on a variety of material platforms, such as perovskite materials, colloidal QDs, conventional semiconductor materials—including InGaAs QWs, InAs/GaAs QDs, and bulk GaAs—as well as other active media. The robust mode confinement capability of BICs enables lasing across diverse material systems. Among these, InGaAsP QW-based BIC lasers have been widely studied, with reported lasing thresholds peak power ranging from 0.45 mW to 73 mW under pulse or CW condition [25, 26, 47]. In contrast, only two works—our own and work [29]—have reported BIC lasers using InAs/GaAs QDs, achieving significantly lower thresholds of 0.0075 mW and 0.017 mW under CW condition. Similarly, the β-factor, which reflects the efficiency of spontaneous emission coupling into the lasing mode, is higher for QD-based lasers (0.05 in our work) compared to QW-based one [26]. This advantage, however, is not solely attributable to material differences, as cavity geometry and mode volume also play critical roles, for example, a coaxial QW-based lasers achieving β-factors as high as 0.99 despite modest Q-factors [21]. Thermal performance further distinguishes QD-based BIC lasers: a recent study [29] reported exceptional thermal stability (0.055 nm/K) over a wide temperature range (273–343 K), a feature not yet demonstrated in QW-based BIC lasers. Moreover, under CW pumping—which imposes a greater thermal load—QD-based devices achieved lasing at thresholds of just tens of microwatts [29] (and our work), compared to higher thresholds in QW-based counterparts [26]. These findings suggest that QD-based BIC lasers may offer superior threshold performance, higher efficiency, and better thermal stability compared to their QW-based counterparts, although a rigorous comparison under identical cavity and excitation conditions is necessary to confirm these advantages.

Our work can be extended to the important case of a BIC laser with electrical injection. To this end, we have come to the conclusion that the design of such a laser is compatible with widely used high-precision fabrication processes. However, the practical implementation of such a BIC laser can be challenging due to the difficulty in balancing the contact area with optical beam aperture. A ring contact design [56, 57] and lateral current injection [58] device configurations are promising solutions to these challenges. The development of an electrically pumped BIC laser requires careful consideration of multiple design aspects, including wafer structure (p-type and n-type doping layers), contact geometry, current path engineering, thermal management, and threshold gain optimization—all of which are essential for enhancing device performance and ensuring reliable operation.

Our on-chip vortex beam laser has the potential to be utilized as a promising light source of OAM-carrying optical beam, which can be employed in on-chip communication systems with large capacity [7, 8]. Moreover, the nontrivial nature of the optical beam, characterized by $+1$ topological charge, makes it particularly robust against perturbations such as optical turbulence. In conjunction with the fact that our laser operates at a wavelength of $\sim$1.3 μm, this robustness vortex optical beam makes our device ideally suitable to be deployed to on-chip communication systems. Other OAM modes with different topological charges can be engineered using similar procedures. It has been theoretically and experimentally demonstrated that BIC-based lasers can generate higher-order OAM modes with various topological charges, determined by the system's rotational symmetry [59]. Demonstrations include lasing with topological charges of -2, -1, and $+1$ [60, 61], highlighting the potential of BIC lasers as compact on-chip vortex beam sources. The BIC laser we developed are expected to extend to even higher-order topological charges by leveraging lattice symmetry and higher-order diffraction. Moreover, our device can be further optimized by increasing the thickness of the airgap, which further reduce the power threshold and increase the Q-factor. Our findings pave the way to engineer an electronic pumping vortex light source with a small footprint and a compact structure.

Table 1. Characteristics of the BIC laser compared with other BIC lasers.

	Pump source	Gain material	Wavelength (nm)	Num. of PC periods	Threshold peak power (mW)	Threshold power density (kW cm^{-2})	Experimental far field pattern	Years
Pulse	$\lambda = 1064$ nm, $T = 12$ ns, repetition rate $f = 275$ kHz	InGaAsP QWs	∼1600 (MM)	N/A	73	—	Doughnut-shaped pattern	2017 [47]
Pulse	$\lambda = 1064$ nm, $T = 12$ ns, repetition rate $f = 300$ kHz	InGaAsP QWs	1551(SM)	∼19 ×19	15.6	∼4	N/A	2017 [25]
Pulse	$\lambda = 780$ nm, $T = 200$ fs, repetition rate of 100 kHz	GaAs bulk	830-850 (MM)	∼200 ×200	8.8 ×10^5	7.0 ×10^4	N/A	2018 [39]
CW	$\lambda = 450$ nm, laser diode	Monolayer WS2	637(SM)	∼100 ×100 (cladding PCs required)		0.144	N/A	2019 [41]
Pulse	$\lambda = 530$ nm, $T = 200$fs, repetition rate of 20 kHz	CdSe/CdZnS NPL	632-663(SM)	—	5.09 ×10^6	1.8 ×10^5	Doughnut-shaped pattern	2020 [43]
Pulse	$\lambda = 400$ nm, $T = 100$fs, repetition rate of 1 kHz	Perovskite	552 (SM)	—	5.28 ×10^5	4.2 ×10^4	Doughnut-shaped pattern	2020 [27]
Pulse	$\lambda = 780$ nm, $T = 120$fs, repetition rate of 1 kHz	IR-792 MOLECULES	∼860 (MM)	—	∼2.16 ×10^6	∼2.75 ×10^4	Doughnut-shaped pattern	2021 [48]
Pulse	$\lambda = 355$ nm, pulse width ∼ 5 ns, repetition rate of ∼1250 Hz	Colloidal quantum dots	∼630 (MM)	∼130 ×130	—	11	Doughnut-shaped pattern	2021 [28]
Pulse	$\lambda = 800$ nm, pulse width 100 fs, repetition rate of 1 kHz	Perovskite	549 (SM)	—		4.9 ×10^5	Two parallel lines	2021 [40]
Pulse	$\lambda = 980$ nm, 2% duty cycle, repetition rate of 1 MHz	InGaAsP QWs	∼1600(SM)	∼23 ×23	0.34	1.47	Doughnut-shaped pattern	2021 [26]
CW	$\lambda = 1480$ nm, laser diode	InGaAsP QWs	∼1560 (SM/MM)	—	3.5	12.38	N/A	2021 [42]
Pulse	$\lambda = 355$ nm, repetition rate of 75 kHz	GaN film	375.8 (SM)	∼40 ×1	2600	—	Circular beam	2023 [30]
CW	$\lambda = 709$ nm, laser diode	InAs/GaAs QD	1311 (SM)	5 ×5 (clad\ding PCs required)	0.017	0.074	N/A	2023 [29]
CW	$\lambda = 709$ nm, laser diode	InAs/GaAs QD	1303/1328 (MM)	7 ×7(cladding PCs required)	0.012	0.052	N/A	2023 [29]
CW	$\lambda = 633$ nm, laser diode	InAs/GaAs QD	1254 (SM)	30 ×30 (no cladding PCs required)	0.0075	0.038	Doughnut-shaped pattern	This work

SM: single mode; MM: multimode; QD: quantum dot; QW: quantum well; PCs: photonic crystals.

Data availability statement

All data that support the findings of this study are included within the article (and any supplementary files).

Supplementary Data available at https://doi.org/10.1088/1361-6463/ae0b80/data1.

Acknowledgments

This work was supported by the National Key R&D Program of China (Grant No. 2023YFB2805900, S. C), Engineering and Physical Sciences Research Council (Grant Numbers EP/Z532848/1, EP/X015300/1, EP/T028475/1 and EP/P006973/1) and SPIKEPro which was received funding from the European Union's Horizon 2020 programme under Grant Agreement Number 101129904.

Author contributions

Danqi Lei 0009-0007-0718-389X
Conceptualization (lead), Data curation (lead), Formal analysis (lead), Investigation (lead), Methodology (lead), Writing – original draft (equal), Writing – review & editing (equal)

Ji Tong Wang
Conceptualization (equal), Data curation (equal), Methodology (equal), Writing – original draft (equal), Writing – review & editing (equal)

Bogdan-Petrin Ratiu
Data curation (equal), Investigation (equal), Methodology (equal), Writing – review & editing (equal)

Huiwen Deng
Methodology (equal)

Xuanchang Zhang 0009-0007-0382-2981
Methodology (equal)

Zhao Yan 0000-0001-5543-6969
Investigation (equal)

Suguo Huo
Investigation (supporting)

Liwei Cao
Investigation (equal)

Wei Li 0000-0002-7411-5519
Investigation (equal), Methodology (equal)

Siming Chen
Methodology (equal), Project administration (equal), Writing – review & editing (equal)

Qiang Li 0000-0001-6875-7403
Funding acquisition (equal), Investigation (equal), Methodology (equal), Project administration (equal), Writing – review & editing (equal)

Huiyun Liu 0000-0002-7654-8553
Conceptualization (equal), Funding acquisition (equal), Investigation (equal), Methodology (equal), Project administration (equal), Writing – review & editing (equal)

Nicolae C Panoiu 0000-0001-5666-2116
Funding acquisition (equal), Investigation (equal), Methodology (equal), Project administration (equal), Writing – review & editing (equal)

Mingchu Tang 0000-0001-6626-3389
Funding acquisition (equal), Investigation (equal), Methodology (equal), Project administration (equal), Supervision (equal), Writing – review & editing (equal)

References

[1] Padgett M and Bowman R 2011 Tweezers with a twist *Nat. Photon.* **5** 343–8
[2] Nicolas A, Veissier L, Giner L, Giacobino E, Maxein D and Laurat J 2014 A quantum memory for orbital angular momentum photonic qubits *Nat. Photon.* **8** 234–8
[3] Musarra G, Wilson K E, Faccio D and Wright E M 2018 Rotation-dependent nonlinear absorption of orbital angular momentum beams in ruby *Opt. Lett.* **43** 3073–5
[4] Tan P S, Yuan X-C, Yuan G H and Wang Q 2010 High-resolution wide-field standing-wave surface plasmon resonance fluorescence microscopy with optical vortices *Appl. Phys. Lett.* **97** 241109–1
[5] Wang J *et al* 2012 Terabit free-space data transmission employing orbital angular momentum multiplexing *Nat. Photon.* **6** 488–96
[6] Wong G K L, Kang M S, Lee H W, Biancalana F, Conti C, Weiss T and Russell P S J 2012 Excitation of orbital angular momentum resonances in helically twisted photonic crystal fiber *Science* **337** 446–9
[7] Bozinovic N, Yue Y, Ren Y, Tur M, Kristensen P, Huang H, Willner A E and Ramachandran S 2013 Terabit-scale orbital angular momentum mode division multiplexing in fibers *Science* **340** 1545–8
[8] Willner A E *et al* 2015 Optical communications using orbital angular momentum beams *Adv. Opt. Photon.* **7** 66–106
[9] Yan W, Chen Z, Long X, Gao Y, Yuan Z, Ren Z-C, Wang X-L, Ding J and Wang H-T 2024 Iso-propagation vortices with OAM-independent size and divergence toward future faster optical communications *Adv. Photon.* **6** 036002
[10] Shen Y, Wang X, Xie Z, Min C, Fu X, Liu Q, Gong M and Yuan X 2019 Optical vortices 30 years on: OAM manipulation from topological charge to multiple singularities *Light Sci. Appl.* **8** 90
[11] Lei T *et al* 2015 Massive individual orbital angular momentum channels for multiplexing enabled by Dammann gratings *Light Sci. Appl.* **4** e257–e
[12] Wang J 2016 Advances in communications using optical vortices *Photon. Res.* **4** B14–B28
[13] Mair A, Vaziri A, Weihs G and Zeilinger A 2001 Entanglement of the orbital angular momentum states of photons *Nature* **412** 313–6
[14] Wang Z, Zhang N and Yuan X C 2011 High-volume optical vortex multiplexing and de-multiplexing for free-space optical communication *Opt. Express* **19** 482–92

[15] Forbes A 2024 On-chip lasers with twisted light *Nat. Photon.* **18** 209–10

[16] Cheng J, Sha X, Zhang H, Chen Q, Qu G, Song Q, Yu S and Xiao S 2022 Ultracompact orbital angular momentum sorter on a CMOS chip *Nano Lett.* **22** 3993–9

[17] Beijersbergen M W, Coerwinkel R P C, Kristensen M and Woerdman J P 1994 Helical-wavefront laser beams produced with a spiral phaseplate *Opt. Commun.* **112** 321–7

[18] Heckenberg N R, McDuff R, Smith C P and White A G 1992 Generation of optical phase singularities by computer-generated holograms *Opt. Lett.* **17** 221–3

[19] He C, Shen Y and Forbes A 2022 Towards higher-dimensional structured light *Light Sci. Appl.* **11** 205

[20] Zhou T *et al* 2020 Continuous-wave quantum dot photonic crystal lasers grown on on-axis Si (001) *Nat. Commun.* **11** 977

[21] Khajavikhan M, Simic A, Katz M, Lee J H, Slutsky B, Mizrahi A, Lomakin V and Fainman Y 2012 Thresholdless nanoscale coaxial lasers *Nature* **482** 204–7

[22] Lin H-T, Hsu K-S, Chang C-C, Lin W-H, Lin S-Y, Chang S-W, Chang Y-C and Shih M-H 2020 Photonic crystal circular nanobeam cavity laser with type-II GaSb/GaAs quantum rings as gain material *Sci. Rep.* **10** 4757

[23] Wan Y, Li Q, Liu A Y, Gossard A C, Bowers J E, Hu E L and Lau K M 2016 Optically pumped 1.3 μm room-temperature InAs quantum-dot micro-disk lasers directly grown on (001) silicon *Opt. Lett.* **41** 1664–7

[24] Zhou Z, Ou X, Fang Y, Alkhazraji E, Xu R, Wan Y and Bowers J E 2023 Prospects and applications of on-chip lasers *eLight* **3** 1

[25] Kodigala A, Lepetit T, Gu Q, Bahari B, Fainman Y and Kanté B 2017 Lasing action from photonic bound states in continuum *Nature* **541** 196–9

[26] Hwang M-S, Lee H-C, Kim K-H, Jeong K-Y, Kwon S-H, Koshelev K, Kivshar Y and Park H-G 2021 Ultralow-threshold laser using super-bound states in the continuum *Nat. Commun.* **12** 4135

[27] Huang C *et al* 2020 Ultrafast control of vortex microlasers *Science* **367** 1018–21

[28] Wu M, Ding L, Sabatini R P, Sagar L K, Bappi G, Paniagua-Domínguez R, Sargent E H and Kuznetsov A I 2021 Bound state in the continuum in nanoantenna-coupled slab waveguide enables low-threshold quantum-dot lasing *Nano Lett.* **21** 9754–60

[29] Zhong H, Yu Y, Zheng Z, Ding Z, Zhao X, Yang J, Wei Y, Chen Y and Yu S 2023 Ultra-low threshold continuous-wave quantum dot mini-BIC lasers *Light Sci. Appl.* **12** 100

[30] Chen M-H, Xing D, Su V-C, Lee Y-C, Ho Y-L and Delaunay J-J 2023 GaN ultraviolet laser based on bound states in the continuum (BIC) *Adv. Opt. Mater.* **11** 2201906

[31] Hsu C W, Zhen B, Stone A D, Joannopoulos J D and Soljačić M 2016 Bound states in the continuum *Nat. Rev. Mater.* **1** 16048

[32] Azzam S I and Kildishev A V 2021 Photonic bound states in the continuum: from basics to applications *Adv. Opt. Mater.* **9** 2001469

[33] Von Neumann J and Wigner E 1929 On some peculiar discrete eigenvalues *Physica Z* **30** 465–7

[34] Zhen B, Hsu C W, Lu L, Stone A D and Soljačić M 2014 Topological nature of optical bound states in the continuum *Phys. Rev. Lett.* **113** 257401

[35] Smowton P M, Sandall I C, Liu H Y and Hopkinson M 2007 Gain in p-doped quantum dot lasers *J. Appl. Phys.* **101** 013107–1

[36] Liu Z *et al* 2020 Origin of defect tolerance in InAs/GaAs quantum dot lasers grown on silicon *J. Lightwave Technol.* **38** 240–8

[37] Tang M, Park J-S, Wang Z, Chen S, Jurczak P, Seeds A and Liu H 2019 Integration of III–V lasers on Si for Si photonics *Prog. Quantum Electron.* **66** 1–18

[38] Shang C, Wan Y, Selvidge J, Hughes E, Herrick R, Mukherjee K, Duan J, Grillot F, Chow W W and Bowers J E 2021 Perspectives on advances in quantum dot lasers and Integration with Si Photonic integrated circuits *ACS Photonics* **8** 2555–66

[39] Ha S T, Fu Y H, Emani N K, Pan Z, Bakker R M, Paniagua-Domínguez R and Kuznetsov A I 2018 Directional lasing in resonant semiconductor nanoantenna arrays *Nat. Nanotechnol.* **13** 1042–7

[40] Wang Y, Fan Y, Zhang X, Tang H, Song Q, Han J and Xiao S 2021 Highly controllable etchless perovskite microlasers based on bound states in the continuum *ACS Nano* **15** 7386–91

[41] Ge X, Minkov M, Fan S, Li X and Zhou W 2019 Laterally confined photonic crystal surface emitting laser incorporating monolayer tungsten disulfide *npj 2D Mater. Appl.* **3** 16

[42] Yu Y, Sakanas A, Zali A R, Semenova E, Yvind K and Mørk J 2021 Ultra-coherent Fano laser based on a bound state in the continuum *Nat. Photon.* **15** 758–64

[43] Wu M, Ha S T, Shendre S, Durmusoglu E G, Koh W-K, Abujetas D R, Sánchez-Gil J A, Paniagua-Domínguez R, Demir H V and Kuznetsov A I 2020 Room-temperature lasing in colloidal nanoplatelets via Mie-resonant bound states in the continuum *Nano Lett.* **20** 6005–11

[44] Liu H Y, Hopkinson M, Harrison C N, Steer M J, Frith R, Sellers I R, Mowbray D J and Skolnick M S 2003 Optimizing the growth of 1.3 μm InAs/InGaAs dots-in-a-well structure *J. Appl. Phys.* **93** 2931–6

[45] COMSOL Multiphysics (available at: https://www.comsol.com/)

[46] Wang T, Liu H, Lee A, Pozzi F and Seeds A 2011 1.3-μm InAs/GaAs quantum-dot lasers monolithically grown on Si substrates *Opt. Express* **19** 11381–6

[47] Bahari B, Vallini F, Lepetit T, Tellez-Limon R, Park J, Kodigala A, Fainman Y and Kante B 2017 Integrated and steerable vortex lasers using bound states in continuum (arXiv:1707.00181)

[48] Mohamed S, Wang J, Rekola H, Heikkinen J, Asamoah B, Shi L and Hakala T 2020 Topological charge engineering in lasing bound states in continuum (arXiv:2012.15642)

[49] Xing D, Chen M H, Wang Z, Deng C Z, Ho Y L, Lin B W, Lin C C, Chen C W and Delaunay J J 2024 Solution-processed perovskite quantum dot quasi-BIC laser from miniaturized low-lateral-loss cavity *Adv. Funct. Mater.* **34** 2314953

[50] Pettine J, Padmanabhan P, Sirica N, Prasankumar R P, Taylor A J and Chen H-T 2023 Ultrafast terahertz emission from emerging symmetry-broken materials *Light Sci. Appl.* **12** 133

[51] Kang M, Liu T, Chan C T and Xiao M 2023 Applications of bound states in the continuum in photonics *Nat. Rev. Phys.* **5** 659–78

[52] Khurgin J B and Noginov M A 2021 How do the Purcell factor, the Q-factor, and the beta factor affect the laser threshold? *Laser Photon. Rev.* **15** 2000250

[53] Coldren L A, Corzine S W and Mashanovitch M L 2012 *Diode Lasers and Photonic Integrated Circuits* vol 218 (John Wiley & Sons)

[54] Yang J-H *et al* 2021 Low-threshold bound state in the continuum lasers in hybrid lattice resonance metasurfaces *Laser Photon. Rev.* **15** 2100118

[55] Willner A E, Pang K, Song H, Zou K and Zhou H 2021 Orbital angular momentum of light for communications *Appl. Phys. Rev.* **8** 041312
[56] Wan Y, Norman J, Li Q, Kennedy M, Liang D, Zhang C, Huang D, Zhang Z, Liu A Y and Torres A 2017 1.3 μm submilliamp threshold quantum dot micro-lasers on Si *Optica* **4** 940–4
[57] Park H-G, Kim S-H, Kwon S-H, Ju Y-G, Yang J-K, Baek J-H, Kim S-B and Lee Y-H 2004 Electrically driven single-cell photonic crystal laser *Science* **305** 1444–7
[58] Matsuo S, Takeda K, Sato T, Notomi M, Shinya A, Nozaki K, Taniyama H, Hasebe K and Kakitsuka T 2012 Room-temperature continuous-wave operation of lateral current injection wavelength-scale embedded active-region photonic-crystal laser *Opt. Express* **20** 3773–80
[59] Yoda T and Notomi M 2020 Generation and annihilation of topologically protected bound states in the continuum and circularly polarized states by symmetry breaking *Phys. Rev. Lett.* **125** 053902
[60] Salerno G, Heilmann R, Arjas K, Aronen K, Martikainen J-P and Törmä P 2022 Loss-driven topological transitions in lasing *Phys. Rev. Lett.* **129** 173901
[61] Zhou X, Li Z, Zhou Y, Bai C and Ao X 2024 Lasing from doubly degenerate bound states in the continuum *J. Phys. Chem. Lett.* **15** 10703–9